Journal of Applied Geodesy 3 (2009), 155–162 © de Gruyter 2009. DOI 10.1515/JAG.2009.016

New parameters of geometrically best fitting lunar figures

H. Bâki Iz

Abstract. The parameters of various lunar figures are of interest to the scientific community working on lunar exploration. In this study, the size of the geometrically best fitting triaxial and rotational ellipsoids, and spheres, are estimated using the method of condition equations with common unknown parameters from the coordinates of 271,610 control points of the newly available lunar control, ULCN 2005. In the first set of solutions, the origin of the figures is calculated with respect to the center of the mass of the Moon. Their origins are set to coincide with the lunar center of mass in the second set of solutions. The new estimates are the most up-to-date values for the triaxial and rotational ellipsoidal and spherical parameters of the lunar figures and are significantly different up to half a km as compared to the most recent solutions.

Keywords. Lunar ellipsoid, lunar sphere, lunar topography, ULCN2005.

Introduction

I wake, and moonbeams play around my bed,
Glittering like hoar-frost to my wandering eyes;
Up towards the glorious moon I raise my head,
Then lay me down – and thoughts of home arise.

Night Thoughts by Li Bai.

The parameters of the various lunar figures are of interest to the scientific community working on lunar exploration. As in the case of the Earth, a mathematical reference surface is required for horizontal lunar control for lunar mapping. The determination of lunar figure parameters has a long history. Analysis of current selenodetic and selenochronological data indicates that the present lunar figure was formed $3.0 \pm 0.5 \times 10^9$ years ago at an earth-moon distance of 20.4 ± 2.3 earth radii (Binder 1982). As early as 350 BC, Aristotle argued that the shape of the moon is a sphere because the boundary of the Sun's light on the moon was always a circular arc. Aristarchus (310–230 BC) also estimated the radius of the moon as 1/3 the radius of the Earth (Schimerman 1973). Extensive information about the history of selenodesy and lunar mapping can be found in Schimerman (1973).

Recent approaches in determining the lunar figure parameters use a spherical harmonic representation of the lunar topography. In an early study, Bills and Ferrari (1977) calculated the axes of a triaxial lunar ellipsoid using a spherical harmonic analysis of lunar topography to degree 12 from Earth based and orbital observations (a, b, and c triaxial ellipsoid lunar axes are 1738.43, 1737.50, 1736.66 km long, respectively, and the mean radius is 1737.53 ± 0.03 km). They determined the offset of the center of the lunar figure from the lunar center of mass to be 1.98 ± 0.06 km toward $(19 \pm 2)^\circ$S, $(194 \pm 1)^\circ$E. In a follow up study, Smith et al. (1997) derived a Goddard Lunar Topography Model (GLTM 2) up to degree and order 72 based on a spherical harmonic expansion of the mass-centered radii deduced from the Clementine radar altimetry measurements. Their analysis of the topographic model with different degree and order long wavelengths (degree and order 2–16) resulted in a number of alternative estimates for the parameters of the lunar figure as a rotational ellipsoid.

Other techniques for determining the lunar figure involve a lunar orbiting satellite moving in the lunar gravitational field with one of its foci at the center of mass of the moon. Its orbit is determined using the earth-based radar tracking. Pictures, such as Lunar Orbiter, of the lunar surface taken from the spacecraft are then related to the position of the spacecraft at the time of exposure using photogrammetric techniques (Ruben 1969), and positions of prominent lunar topographic features that appear on the pictures are calculated. The position information is subsequently used to calculate the lunar figure.

The approach used to calculate the lunar figures in this study exhibits similarities with the later method. A fortuitous byproduct of the recent Unified Lunar Control, known as ULCN 2005 solution, is the availability of densely distributed 3D lunar control, which were photogrammetrically determined, and improved with the fusion of 2D ULCN 1994, and Clementine Lunar Control Networks (CLCN). In this study, the best fitting lunar figure parameters for selenocentric and non-selenocentric triaxial and rotation ellipsoids and spheres (a total of six figures) were estimated by solving the condition equations for each one of 271,610 control points, while accounting for the least-square adjustment of the 814,830 *Cartesian* coordinates of the ULCN 2005 control stations.

Lunar Control Networks

The recent lunar control networks include the Unified Lunar Control Network (ULCN 1994) and the Clementine Lunar Control Network (CLCN), both derived at RAND (Davies, et al. 1994), and ULCN 2005 at USGS (Archinal et al. 2005, 2006). The ULCN 1994 was based on the images from the Apollo, Mariner 10, and Galileo missions, and Earth-based photographs whereas the CLCN was derived from Clementine images and measurements on Clementine 750-nm images (Edwards, et al. 1996). Further information about these solutions can be found in USGS Astrogeology site (USGS, Control Networks 2008).

ULCN 2005 is the fusion of the ULCN 1994 and CLCN improving greatly upon the accuracy of the CLCN. The primary significant feature of the ULCN 2005 in comparison to the previous networks is due to the radii of the control points being included in the solution. Hence, the resulting ULCN 2005 is a unified three dimensional photogrammetrically determined network, which consists of 272,931 control points with an average of one point for every approximately 46 km^2 (Archinal et al. 2006). Comparison by Archinal et al. (2006) revealed that the radii derived from the images show no systematic difference between the Clementine LIDAR values (Smith et al. 1997), which implies that the radii must be of a few hundred meters accuracy of LIDAR. The horizontal accuracy of the ULCN is also reported to be a few hundred meters (Archinal et al. 2006).

The lunar control networks can be referenced to two slightly different lunar body-fixed coordinate systems: *a mean Earth/rotation system*, and *a principal axis system* (Roncoli 2005). The mean Earth/polar axis system (also called the *mean Earth/rotation system*) is a *lunar body-fixed* coordinate system based upon a mean direction to the Earth and a mean axis of rotation of the Moon. The principal axis system is also a lunar body-fixed coordinate system aligned with the *principal axes* of the Moon. The principal axes and the mean Earth/rotation axes of the Moon do not coincide but differ by less than 1 km because the Moon is not really a synchronously rotating triaxial ellipsoid (ibid). In this system, the mean Earth equator is defined at J2000 with the origin at the center of mass of the Moon. The selenocentric latitudes are measured from the center of the Moon relative to the equator and longitudes are measured from 0–360 degrees, positive to the east with the exception that nearly all of the lunar maps depict longitudes as both east and west longitudes. Data fusion CLCN in ULCN 2005 solution with ULCN 1994, and the use of Clementine a priori spacecraft position data in the mean Earth/polar axis system ensures that ULCN 2005 is referenced to the same mean Earth/polar axis system reported in Davies et al. (1994), Archinal et al. (2005).

Solutions

Three variants of lunar figures were considered: A triaxial spheroid with figure semi-axes *a, b, and c* is represented with the following condition equation, which include the unknown *non-selenocentric* lunar figure parameters,

$$\frac{(x-x_c)^2}{a^2}+\frac{(y-y_c)^2}{b^2}+\frac{(z-z_c)^2}{c^2}-1=0. \quad (1)$$

A special case of (1) with semi-major axis $a = b$, and semi-minor axis c represents a rotational ellipsoid (no a priori constraints are to be used to ensure that $a > c$ in estimating the lunar figure parameters. Hence, the model represents a rotationally *oblate* as well as a *prolate* ellipsoid), and a sphere with a radius, $a = b = c = R$. The origins of all of the above geometric figures are located at x_c, y_c, z_c with respect to the underlying coordinate system. If $x_c = y_c = z_c = 0$, then the geometric centers of the figures are constrained to coincide with the origin of the coordinate system. In this case the lunar figure parameters refer to the selenocentric lunar shapes. The lunar figure parameters *a, b, c* are the semi-axes, towards the Earth, in the plane of the sky perpendicular to, and along the polar axis respectively.

Condition equation (1) and all its variants are *non-linear* and contain 3D coordinates of control stations as observations. The observations are adjusted due to the observation error, together with the unknown lunar figure parameters were estimated by minimizing the *Lagrangian* target function with condition equations using an iterative algorithm (Pope 1972). Although the number of unknown lunar figure parameters in each formulation are small (largest being 6, 3 for size, and 3 for the origin of a triaxial ellipsoid), there are 271,610 control points and the same number of condition equations – one for each control point – to be formulated, and 814,830 observations (three coordinate components for each control) to be adjusted – substantially large in number. A partitioned computational formulation (Appendix A) significantly reduced the storage requirements during the computations. The viable sub-matrices for partitioned numerical solutions consist of 10 control points leading to 30 linearized condition equations with common unknown parameters within each partition. The vector norm of the vector of the estimated corrections to the unknown parameters converged to less than a mm after the third iteration for all the solutions for the non-selenocentric and selenocentric best fitting triaxial, rotational ellipsoids and spheres. In all these solutions, an identity matrix was used for the weigh matrix. An alternative set of solutions were also obtained using an iteratively weight least squares version of the least squares solution. The weight matrix for each iteration is calculated from the inverse residual squares of the adjusted control points' *Cartesian* coordinates of an earlier iterative solution. This solution methodology is more robust to the influence of the large topographical features on the moon because the control points located in these areas are down weighted by their correspondingly large residuals.

Table 1 lists all the estimated parameters for selenocentric lunar and non-selenocentric lunar figures. The differences between the parameters of the selenocentric and non-selenocentric parameters for the same figures are not significantly different despite the

Table 1: Units are in meters. The values within parentheses are the standard errors of the estimated parameters. The first set of values of each lunar figure parameters belongs to the non-selenocentric best fitting lunar figure, whereas the second sets are calculated using iteratively reweighted least squares solution. The third set of values is the corresponding parameters reported by the most recent solutions by Smith et al. (1997). The last set of values is the selenocentric solutions. Hyphens are for the missing values of earlier solutions. Because iteratively reweighted solutions use inverse residual squares as weights, the variance factor (a posteriori variance of unit weight) is always close to unity; hence, the standard errors of the parameters are not precisely represented. N/A stands for not applicable.

Figure	a	b	c	x_c	y_c	z_c	RMS
Triaxial	1737899(9)	1737570(9)	1735742(7)	−1658(6)	−681(6)	133(5)	1754
Ellipsoid	1737900(–)	1737570(–)	1735743(–)	−1657(–)	−681(–)	133(–)	1842
	1737811(10)	1737595(10)	1735710(8)	0	0	0	2018
	1738056(17)	1737843(17)	1735485(72)	0	0	0	–
Rotational	1737737(5)	N/A	1735741(7)	−1653(6)	−682(6)	133(5)	1756
Ellipsoid	1737738(–)	N/A	1735742(–)	−1652(–)	−681(–)	134(–)	1844
	1737705(6)	N/A	1736710(8)	0	0	0	2018
	1738208(–)*	N/A	1736261(–)	0	0	0	–
Sphere	1736965(6)	N/A	N/A	−1645(6)	−696(7)	142(6)	1868
	1736966(–)	N/A	N/A	−1644(–)	−696(–)	142(–)	1963
	1736934(4)	N/A	N/A	0	0	0	2117
	1737103(15)	N/A	N/A	0	0	0	–

* (16 × 16) degree and order harmonic solution of Smith et al. (1997).

estimated geometric center offsets being as large as 1.7 km for the x components. The estimated offsets are only few meters different for the lunar figures. The uncertainties of the estimated parameters remain within the 4–10 m range for all the solutions.

The *Cartesian* coordinate components' residuals of the control points exhibit a bell-shaped distribution, which can be observed in the histogram for the non-selenocentric rotational ellipsoid solution in Figure 1. All the coordinate components are distributed similarly within each bin with close to 22 percent of them falling within ±200 m interval. Note that the large tail values are the cumulative effect of open-ended bin intervals at the tail bins – not a property of the solution.

The RMS residuals for each *Cartesian* component are close to one km (Table 2), and show a balanced distribution of residuals among the station coordinates. However, RMS values are considerably large (up to 1 km) because of the lunar topography. All the lunar mathematical figures favor intrinsically the radial component of the topography. Consider for instance the formulation of the selenocentric spherical lunar figure for which the corresponding condition equation reduces to $(x^2 + y^2 + z^2) - R^2 = 0$. Its least-squares solution is tantamount to minimizing

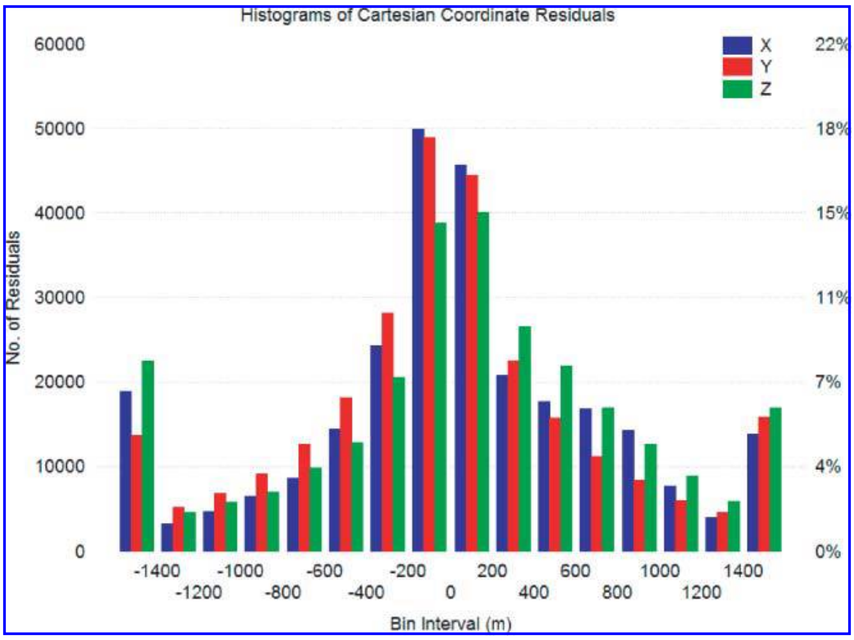

Figure 1: Distribution of the X, Y and Z coordinate components' residuals of the control points. Solution model is the non-selenocentric rotational ellipsoid.

Table 2: The RMS residual statistics for the Cartesian and projected latitudinal, longitudinal, and radial components from the non-selenocentric best fitting rotational ellipsoid solution.

Residual Component	RMS (m)
X	1033
Y	821
Z	1158
Latitudinal	2
Longitudinal	17
Radial	1756

the difference between the square of the unknown spherical radius parameter, R, and the square of the radial distance calculated from the *Cartesian* components, x, y, z of a control station. Consequently, the RMS residuals cannot be effectively reduced to a level to reflect the accuracy or precision of the solutions based solely on the observational errors in the coordinates because of the presence of the lunar topography in the radial values. The histogram of the radial residuals (Figure 2), which are calculated from the *Cartesian* coordinate components using the relationships given in Appendix B, shows that approximately 70% of them fall within $[-1, 1]$ km interval. This ambiguity is also observed in the determination of the lunar figure from the harmonic representation of topography in earlier solutions. The determination of lunar figure parameters using different wavelengths, for instance, led to different estimates of the lunar figure parameters in Smith et al. (1997).

For the current solutions, the RMS residuals range within 1.7–2.1 km interval (Table 1), which is mostly a summary measure of the roughness of the lunar topography. Nonetheless, all the solutions can still be contrasted for the best fitting lunar figure as long as they use the same data.

Table 2 also lists the RMS residuals of the station positions in the latitudinal, longitudinal and in the radial directions, which are calculated from the residuals of the *Cartesian* station coordinates. The RMS residuals in the radial directions now quantify the prominence of the topography in this direction, as discussed previously, which are larger than the latitudinal and longitudinal residual components by an order of 1000, as shown in Figure 1 by different bin scales.

Figure 3 shows the misclosures (scaled by the radius of the moon in order to quantify otherwise the unitless values) calculated using the condition equation for the non-selenocentric rotational ellipsoid. Misclosures, as opposed to radial residuals, also include the effect of the latitudinal and longitudinal residual components albeit their negligibly small contributions. Again, the topography, as reflected in Figure 3, is the main source of variability in misclosures.

Conclusion

Although a meaningful statistical testing of the solution results to identify the best fitting lunar figure is not possible because of the presence of the lunar topography in the residuals (unless a stochastic process to the lunar topography is justifiably prescribed), it is observed that the RMS residuals favor systematically the non-selenocentric lunar figures (Table 2). Whereas the RMS differences within the three non-selenocentric solutions are negligibly small, especially between the triaxial and rotation ellipsoid solu-

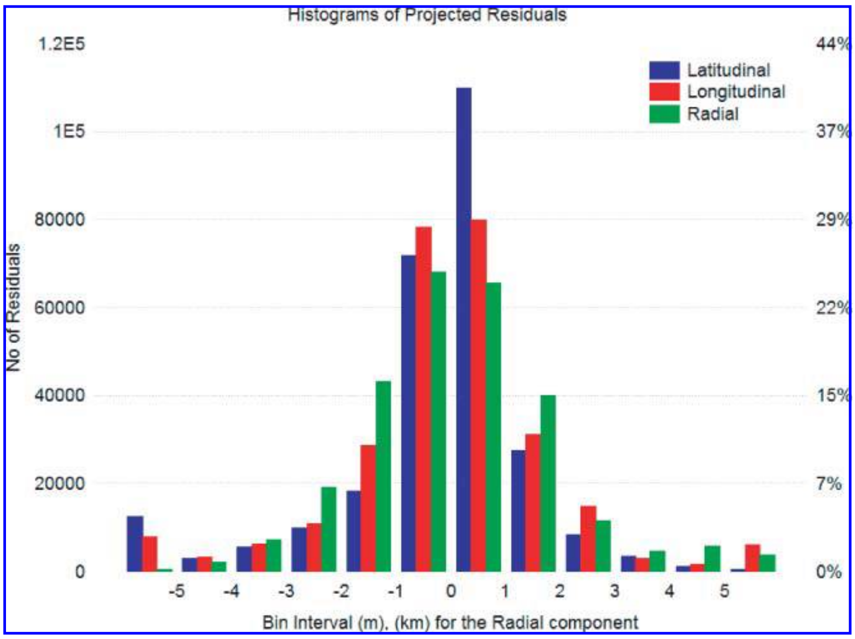

Figure 2: Distribution of the Cartesian residuals of the control points projected in the latitudinal, longitudinal, and radial directions. Bin intervals are in meters for the latitudinal, longitudinal and in kilometers for the radial residuals. The solution model is the non-selenocentric rotational ellipsoid.

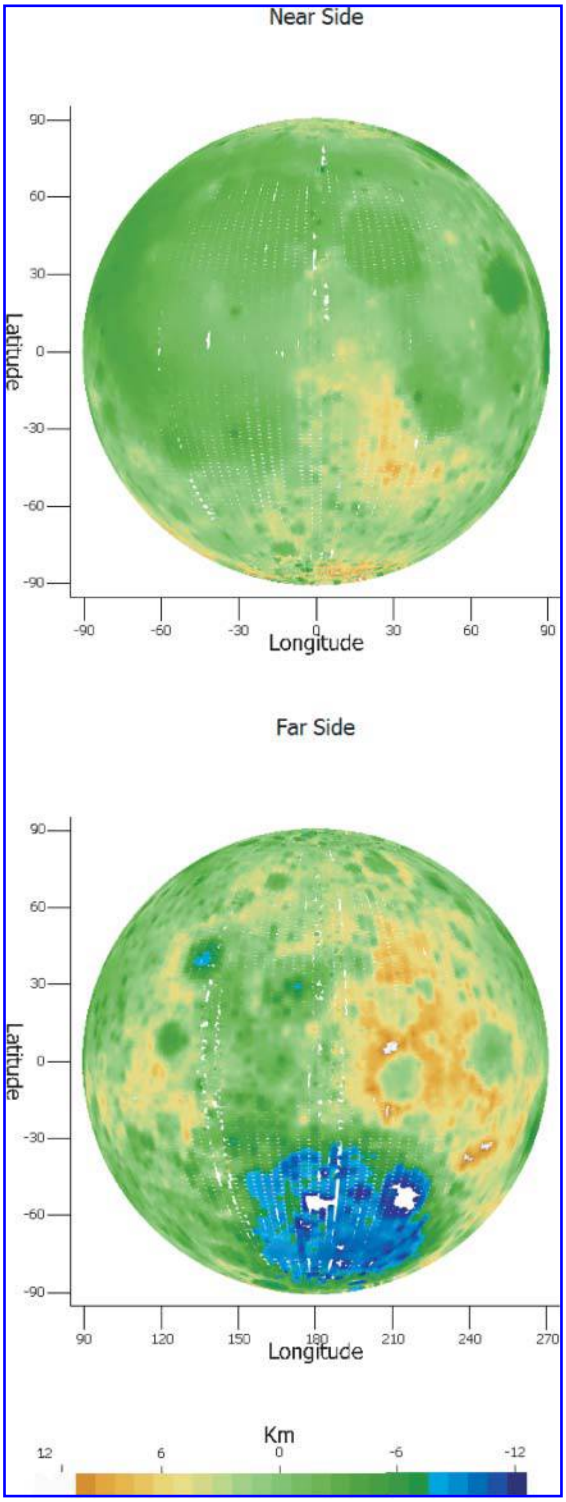

Figure 3: Misclosures of the best-fitting solution for the non-selenocentric rotational ellipsoid model are calculated using equation (1). The deviations from unity are multiplied by an average radius of the moon to provide scale in km. They are shown on a modified orthographic projection for the near (top) and far side of the moon.

tions (about 2 m). Hence, in conclusion, the non-selenocentric rotational ellipsoid, which offers a simpler lunar figure, is preferable.

All the solutions presented in this study provide the most updated parameters about the lunar figures and serve as a mean of summarizing the properties of the lunar surface shape as revealed by the control network. The new estimates are also significantly different as compared to the most recent solutions by Smith et al. (1997). The difference is about 170 m in the spherical radius for the selenocentric solutions. The triaxial selenocentric solutions differences are much larger, 157, 258 and 225 m for the axial parameters a, b, and c respectively. The largest differences are obtained for the rotational ellipsoid parameter reaching 503 and 449 m for the semi-major and semi-minor axes (Table 1).

The offsets of the lunar figures geometric centers from the center of mass of the Moon by several hundred meters (Table 1) are more likely due to the variation in crustal thickness and density of the Moon. Large topographic features such as nearside maria in the northern hemisphere and the large South Pole Aitken Basin on the far side of the moon, do not contribute significantly to the offsets as evidenced by small changes between regular and iteratively reweighted solutions. The latter down weights the control points with large residuals due to the topography in the solutions.

Although the data used in this study are not independent of the data used in the earlier solutions, the changes are because of the complete coverage of the ULCN 2005 solutions, hence a better geometry and the density of the ULCN 2005 data a result of the fusion of larger number of data in its construction. For the very same reason, the inclusion of the new data from the new missions will have predictable impact on the current solution precisions because of the already overwhelming number of data used in estimating the lunar figure parameters (the square root effect). The solution statistics will change significantly only if the existing control point coordinates are projected onto an adopted smooth reference equipotential surface, an adopted geoid-like equipotential surface for the vertical lunar control, as demonstrated by varying estimates in the solutions generated by Smith et al. (1995) using different harmonic representations of the lunar topography. Nonetheless, the calibration of the ULCN 2005 control networks using the *Chang'E-1*, *SELENE* and *Chandrayaan-1* missions' data will contribute to the accuracy of the estimated parameters, or better, they will significantly improve the density of the current lunar control.

As pointed out by the reviewers, additional solutions, which account for the orientation of best fitting lunar figures with respect to the mean Earth/rotation system, are also desirable to gain insight about the geophysical properties of the Moon. These new solutions are underway using the newly acquired *Chang'E-1* laser altimetry measurements.

Appendix A: Condition equations with common unknown parameters and their weighted and iteratively reweighted least squares solutions

We consider the following *non-linear* mathematical model that contains observations y, as well as the unknown parameter x:

$$F(y, x) = 0. \tag{2}$$

A linear model is obtained using *Taylor's* series expansion and omitting all higher than the first order terms,

$$\frac{\partial F}{\partial y} v + \frac{\partial F}{\partial x} \delta x + F(y, x^0) = 0 \tag{3}$$

where x, $\tilde{x}$, x^0 denote the theoretical, estimated and nominal (approximate) values of the unknown parameters, y, $\tilde{y}$, y^0 are the observed, adjusted and approximate values of the observations with *residuals* v and,

$$\tilde{y} = y + v, \tag{4}$$

$$\tilde{x} = x^0 + \delta x, \tag{5}$$

$$B := \left.\frac{\partial F}{\partial y}\right|_{y^0, x^0}, \quad A := \left.\frac{\partial F}{\partial x}\right|_{y^0, x^0}. \tag{6}$$

The partials are evaluated using the observed values for the observations and the approximate values for the parameters y^0 and x^0 respectively. Hence, the *misclosure* vector w is given by

$$w := F(y, x^0) \tag{7}$$

for $y^0 = y$. The partials given by (6) are evaluated by using the observations and the nominal values for the unknown parameters. However, because the solution to the above linearized condition equation is iterative; the misclosure vector must be calculated using the following expression in subsequent steps (Pope 1972):

$$w := F(\tilde{y}, x^0) - Bv \tag{8}$$

using the residuals and the partials evaluated at the *adjusted* values of the observations, both calculated at the end of the previous iteration.

We write the above equation in matrix notation for n observations with r conditions equations that contain u common unknown parameters as follows:

$$\underset{r\times n}{B}\, \underset{n\times 1}{v} + \underset{r\times u}{A}\, \underset{u\times 1}{\delta x} + \underset{r\times 1}{w} = \underset{r\times 1}{0}. \tag{9}$$

The weight matrix associated with the observations is denoted by $\underset{n\times n}{P}$. The principle of the minimum variance solution requires minimizing the $v^T P v$ and fulfilling the conditions imposed on the observations can be obtained using the method of *Lagrange* multipliers for the following target function:

$$\phi = v^T P v - 2\lambda^T (Bv + A\delta x + w) = \text{stationary}, \tag{10}$$

where λ is a $n \times 1$ vector of *Lagrange* multipliers. The solution includes the following compendium of equations (ibid).

The unknown parameters can be calculated using the following expression:

$$\delta x = -(A^T M^{-1} A)^{-1} A^T M^{-1} w \tag{11}$$

with the corresponding variance/covariance matrix

$$\Sigma_{\tilde{x}} = \Sigma_{\delta x} = \tilde{\sigma}_0^2 (A^T M^{-1} A)^{-1}, \tag{12}$$

where $M := BP^{-1}B^T$.

The *Lagrange* multiplier vector

$$\lambda = -M^{-1}(A\delta x + w) \tag{13}$$

can be used in the calculation of the residuals and the a posteriori variance of the unit weight $\tilde{\sigma}_0^2$ as follows:

$$v = P^{-1} B^T \lambda = -P^{-1} B^T M^{-1} (A\delta x + w) \tag{14}$$

$$\Rightarrow v^T P v = -\lambda^T w, \tag{15}$$

$$\tilde{\sigma}_0^2 = \frac{v^T P v}{r - u}. \tag{16}$$

The number of unknown lunar figure parameters in each formulation is small (largest being 6, 3 for size, and 3 for the origin of a triaxial ellipsoid). Yet there are 271,610 control points and the same number of condition equations – one for each control point – to be formulated and 814,830 observations (three coordinate components for each control) to be adjusted – substantially large in number. The following partitioned computational formulations significantly reduce the storage requirements during the computations.

Linearized condition equations given by (9) can be arranged into k groups with p condition equations in each group:

$$\begin{gathered} \underset{p\times 3p}{B_1}\, \underset{3p\times 1}{v_1} + \underset{p\times u}{A_1}\, \underset{u\times 1}{\delta x} + \underset{p\times 1}{w_1} = \underset{p\times 1}{0}, \\ \vdots \\ \underset{p\times 3p}{B_k}\, \underset{3p\times 1}{v_k} + \underset{p\times u}{A_k}\, \underset{u\times 1}{\delta x} + \underset{p\times 1}{w_k} = \underset{p\times 1}{0}. \end{gathered} \tag{17}$$

Assuming that the observations from group-to-group are uncorrelated, the following partitions are obtained,

$$A = \begin{bmatrix} A_1 \\ \vdots \\ A_p \end{bmatrix}, \quad B = \begin{bmatrix} B_1 & \cdots & 0 \\ \vdots & \ddots & \vdots \\ 0 & \cdots & B_p \end{bmatrix}, \tag{18}$$

$$P = \begin{bmatrix} P_1 & \cdots & 0 \\ \vdots & \ddots & \vdots \\ 0 & \cdots & P_p \end{bmatrix}, \quad w = \begin{bmatrix} w_1 \\ \vdots \\ w_p \end{bmatrix} \tag{19}$$

$$\Rightarrow M = BP^{-1}B^T = \begin{bmatrix} B_1 P_1^{-1} B_1^T & \cdots & 0 \\ \vdots & \ddots & \vdots \\ 0 & \cdots & B_k P_k^{-1} B_k^T \end{bmatrix} \tag{20}$$

$$\Rightarrow M^{-1} = \begin{bmatrix} (B_1 P_1^{-1} B_1^T)^{-1} & \cdots & 0 \\ \vdots & \ddots & \vdots \\ 0 & \cdots & (B_k P_k^{-1} B_k^T)^{-1} \end{bmatrix} \tag{21}$$

$$\Rightarrow \begin{aligned} A^T M^{-1} A &= \sum_{i=1}^{k} A_i^T M_i^{-1} A_i, \\ A^T M^{-1} w &= \sum_{i=1}^{k} A_i^T M_i^{-1} w_i. \end{aligned} \tag{22}$$

Hence,

$$\begin{aligned} \delta x &= -\left[\sum_{i=1}^{k} A_i^T M_i^{-1} A_i\right]^{-1} \sum_{i=1}^{k} A_i^T M_i^{-1} w_i \\ &\rightarrow \tilde{x} = x^0 + \delta x, \end{aligned} \tag{23}$$

$$\Sigma_{\tilde{x}} = \tilde{\sigma}_0^2 \left[\sum_{i=1}^{k} A_i^T M_i^{-1} A_i\right]^{-1}. \tag{24}$$

Similarly, it can be shown that

$$\begin{aligned} \lambda &= -M^{-1}(A\delta x + w) \\ &= -\begin{bmatrix} M_1^{-1}(A_1 \delta x + w_1) \\ \vdots \\ M_k^{-1}(A_k \delta x + w_k) \end{bmatrix} =: \begin{bmatrix} \underset{p\times 1}{\lambda_1} \\ \vdots \\ \underset{p\times 1}{\lambda_k} \end{bmatrix} \end{aligned} \tag{25}$$

$$\Rightarrow v = P^{-1} B^T \lambda = \begin{bmatrix} P_1 B_1^T \lambda_1 \\ \vdots \\ P_k B_k^T \lambda_k \end{bmatrix} \tag{26}$$

$$\Rightarrow v^T P v = -\lambda^T w = \sum_{i=1}^{k} \lambda_i w_i. \tag{27}$$

Alternatively, an iteratively weighted least squares solution can also be used to solve the linearized mathematical model given by equation (9) by defining the weight matrix, P, using the inverse residual squares of the adjusted control points (*Cartesian* coordinates) calculated during the iterations. An identity matrix is used for the weight matrix in the first iteration. The inverse residual squares of the adjusted control points' Cartesian coordinates, calculated during the first iteration, are used as weights in the second iteration. Iterations continue until the norm of the corrections to the approximate values of the adjusted parameters converges to zero and the sum of the residual squares stabilizes. Note that since the weights are formed using the inverse residual squares, the weighted sum squares of the residuals are always close to one, hence the *a posteriori* variance of unit weight (variance factor) cannot be used to scale the variance covariance matrix of the adjusted lunar figure parameters.

Appendix B: Residual transformation

We would like to transform the *Cartesian* coordinate residuals v_x, v_y, v_z, to the selenocentric residuals v_r, v_φ, v_λ of selenocentric coordinates – radial, latitudinal and longitudinal counterparts.

Consider the following relationships between the selenocentric coordinates (r, φ, λ) and the corresponding *Cartesian* coordinates (x, y, z) of a point in the selenocentric coordinate system,

$$\begin{bmatrix} x \\ y \\ z \end{bmatrix} = \begin{bmatrix} r\cos\phi\cos\lambda \\ \cos\phi\sin\lambda \\ r\sin\phi \end{bmatrix}. \tag{28}$$

From which, by partial differentiation, the differential changes in these coordinates that approximate the *Cartesian* coordinate residuals v_x, v_y, v_z and v_r, v_φ, v_λ are given by

$$\begin{bmatrix} v_x \\ v_y \\ v_z \end{bmatrix} = \begin{bmatrix} \cos\phi\cos\lambda & -r\cos\phi\sin\lambda & r\sin\phi\cos\lambda \\ r\cos\phi\sin\lambda & r\cos\phi\cos\lambda & r\sin\phi\sin\lambda \\ \sin\phi & 0 & -r\cos\phi \end{bmatrix} \cdot \begin{bmatrix} v_r \\ v_\lambda \\ v_\phi \end{bmatrix}. \tag{29}$$

Its inversion gives the following desired transformation equations,

$$\begin{bmatrix} v_r \\ v_\lambda \\ v_\phi \end{bmatrix} = \begin{bmatrix} \cos\phi\cos\lambda & \cos\phi\sin\lambda & \sin\phi \\ -\dfrac{\sin\lambda}{r\cos\phi} & \dfrac{\cos\lambda}{r\cos\phi} & 0 \\ -\dfrac{\sin\phi\cos\lambda}{r} & -\dfrac{\sin\phi\sin\lambda}{r} & \dfrac{\cos\phi}{r} \end{bmatrix} \begin{bmatrix} v_x \\ v_y \\ v_z \end{bmatrix}. \tag{30}$$

Acknowledgement

This study was supported by the Hong Kong Polytechnic University grants G-U417 and 1-BB83. UCLN 2005 data and pertinent information were provided by Brent Archinal from USGS, which is gratefully acknowledged. I wish to thank two anonymous reviewers for their careful reading of the manuscript and their comments.

References

Archinal, B. A., Rosiek, M. R., Kirk, R. L., and Redding, B. L., The Unified Lunar Control Network 2005, U.S. Geological Survey Open-File Report (2006), 2006–1367.

Army Map Serv. and Aeronaut. Chart Inform. Center, Department of Defense Selenodetic Control System Tech. Rep. No. 1, Def. Intel. Agency, 1966.

Bills, B. G., and Ferrari, A. J., A harmonic analysis of lunar topography, Icarus 31, (1977), 224–259.

Binder, A. B., The Moon: Its Figure and Orbital Evolution, GRL 9:1 (1982), 33–36.

Davies, M. E., Colvin, T. R., and Meyer, D. L., A unified lunar control network: the near side, JGR 92 (1987), 14177–14184.

Edwards, K. E., Colvin, T. R., Becker, T. L., Cook, D., Davies, M. E., Duxbury, T. C., Eliason, E. M., Lee, E. M., McEwen, A. S., Morgan, H., Robinson, M. S., and Sorensen, T., Global Digital Mapping of the Moon, Lunar Planet. Sci. 27 (1996), 335.

Pope, A. J., Some Pitfalls to be Avoided in the Iterative Adjustment of Nonlinear Problems, Proc. 38th An. Meet. Am. Soc. Phot., 1972.

Roncoli, R. B., Lunar Constants and Models Document, JPL D-32296, 2005.

Ruben, L. J., An Analytical Study of Lunar Surface Shape and Size From Lunar Orbiter Mission I Photographs, NASA Technical Note NASA JT D-5243, 1969.

Schimerman, L. A. (ed.), Lunar Cartographic Dossier, Volume I, NASA and the Defense Mapping Agency, St. Louis, Missouri. With changes and additions to 1977 July. 1973.

Smith, D. E., Zuber, M. T., Neumann, G. A., and Lemoine, F. G., Topography of the Moon from the Clementine LIDAR, JGR 102 (1997), 1591–1611.

USGS Control Networks, http://astrogeology.usgs.gov/Projects/ControlNetworks/ (accessed Jan 2008).

Received: Jan 30, 2009 Accepted: Apr 11, 2009

Author information
H. Bâki Iz
Department of Land Surveying and Geo-Informatics
The Hong Kong Polytechnic University
Hong Kong S.A.R., China
E-mail: lshbiz@polyu.edu.hk